Numerical Simulations of Fan/Airframe Interaction with Active Flow-Control

Fulvio Sartor, Alan Burlot, Michaël Méheut

Numerical Simulations of Fan/Airframe Interaction with and without Active Flow-Control

F. Sartor,* A. Burlot,† M. Méheut,‡

ONERA - The French Aerospace Lab, F-92190 Meudon, France

This paper presents a numerical study of a Ultra High Bypass Ratio turbofan (UHBR) with and without active flow control in isolated conditions. Steady and unsteady Reynolds-Averaged Navier-Stokes equations are solved on a 360° representation of the isolated engine, where the rotating fan and the outlet guide vane (OGV) are fully modelled to analyse the interaction with the airframe. Spatial and temporal resolution are discussed, and different approaches are proposed providing increasing levels of fidelity. The configuration is first investigated without control for various angles of attack at low-speed conditions. Then, the angle of attack is increased until massive flow detachment is observed, and active flow-control technique is proposed to mitigate the impact of the separated zone using flow-suction upstream of the fan. A parametric study is proposed using steady-state simulations, aiming at evaluating the most efficient configuration that allows a gain in the overall performance of the engine while limiting the costs induced by the control device. This work has been conducted in the framework of the European funded Clean Sky 2 project ASPIRE, aiming at demonstrating the ability of existing numerical and experimental methods to accurately assess the aerodynamic and acoustic performance of UHBR engines thanks to a reliable modelling of fan/airframe physical interactions.

I. Introduction

Reduction of fuel consumption and environmental impact are driving the design of the current engines for civil aviation. Increasing the bypass ratio further towards UHBR technology is expected to bring substantial improvement. The use of innovative technologies, such as new light-weight materials, allows a shift to higher values of the optimal bypass ratio, which is driven by a compromise between propulsive efficiency, aerodynamic drag and weight. Reaching this high BPR leads to a major modification in the nacelle and fan designs. In order to increase the flow in the secondary duct, the diameter of the nacelle must be increased, while the length is reduced to limit the overall weight. This reduction leads to a diminution in the air intake length, which is designed to stabilize the flow in front of the fan blades. These modifications may have a strong impact on the aerodynamic field in the intake and could lead to a loss of performance and undesirable flow separation upstream of the fan.

The design of this new type of UHBR engines is a complex process, where multiple elements composing the turbofan have to be adapted in order to find the most efficient solution that satisfy the requirements. The interaction between the main elements composing the engine (intake, fan, OGV, nozzle) can lead to a complex flow field: the non axial-symmetric geometry of the nacelle implies that the flow is three-dimensional even at zero angle of attack. In addition, design at take-off conditions must take into account the high angle of attack of the incoming flow, leading to a highly three-dimensional field. The consequence is the need of a 360° representation of the whole configuration, where each fan and OGV blade is modelled inside the engine. Many low-fidelity approaches are currently used to evaluate the overall performance of the turbofan,[1] but they often come with hypothesis that limit the application for complex cases where an accurate description is needed, for example when a high angle of attack produces a massive separation that is ingested by the fan. In addition, the flow inside the engine is unsteady, and time-accurate simulations are necessary to reproduce the interaction between the flow around the rotating fan and the rest of the stationary engine.

*Research Scientist. Aerodynamics, Aeroelasticity and Acoustics Department (DAAA); fulvio.sartor@onera.fr
†Research Associate. Aerodynamics, Aeroelasticity and Acoustics Department (DAAA)
‡Research Scientist. Aerodynamics, Aeroelasticity and Acoustics Department (DAAA); michael.meheut@onera.fr

The intake is usually designed to have high-efficiency in cruise conditions, where the incoming flow is uniform and normal to the fan face. However, the intake must be capable of providing the fan with as uniform flow as possible also in other conditions, for example take-off with cross wind. In this case the angle of attack of the engine can be high and, for an installed engine, this is even locally increased by the deflection caused by the wing, so even more severe incidences must be considered in the design process. Intakes designed for cruise condition are prone to separation at high angle of attack. For the UHBR engines considered in this study, the length of the intake duct is reduced, and the separation is ingested by the fan. This represent a strong limit for the overall performance of the engine (surge can appear) and is a dimensioning factor for the structural strength of the fan blades. Thus, reducing the separation in short intakes has an interest for the design of new engines, where a compromise must be found between short inlets, with limited drag at cruise, and separation-free inlets at take-off, with better propusion efficiency at high angles of attack.[2]

The suppression of flow separation by active flow control techniques is a promising technology for future transport aircraft[3] and is subjected to a growing interest even for industrial applications.[4] In the past years, noise reduction techniques have been proposed for high-bypass ratio engines, and many efforts have led to the currently implemented solution based on passive devices.[5] Active flow-control devices, such as fluidic systems made of impinging micro jets, have also been proposed for high BPR engines.[6] Another solution, commonly used for laminar flow control,[7] is boundary-layer suction through porous walls. It has been shown that this method can be applied not only for drag-reduction purposes, but also for separation control.[8] Additionally, in the case of shock-wave/boundary-layer interaction, it has been proven that shock-induced separation can be more effectively controlled via downstream suction rather than mechanical vortex generators, or impinging micro jets in the incoming supersonic boundary layer.[9]

In this paper we will consider an isolated UHBR turbofan, representative of a modern engine typical of a large passenger aircraft. The elements composing the engine, such as the intake, each fan and OGV blades and the nozzle, are geometrically represented. The configuration is numerically investigated with both steady-state and time-accurate RANS at increasing incidence. The configuration is firstly considered without flow control, where massive separation appear when the angle of attack is high. For the most separated case, flow-control is considered, and a parametric study is proposed in order to find the most efficient configuration that allows a gain in the overall performance of the engine while limiting the cost of the control device.

The activities presented in this paper were conducted in the frame of the European Clean Sky 2 project ASPIRE in collaboration with Airbus, DLR and NLR. The test case is a 360° representation of the turbofan, presented in Section II with a description of the meshing strategy as well as the numerical approach used for the computational fluid dynamics. The steady-state and time-accurate solutions obtained solving RANS equations are first presented in Section III for the configuration without control devices, then with flow control in Section IV. Particular attention is given to the evaluation of the overall aerodynamic performances of the controlled and uncontrolled cases, aiming at assessing the efficiency of the proposed flow-control technique. Section V will summarise the results of the investigation.

II. Numerical approach

The configuration investigated in this paper is depicted in figure 1. It is composed of an isolated double-stream turbofan with a bypass ratio around 16. The diameter of the nacelle is higher than in conventional engines, the fan is composed of 16 blades and 36 OGV are present downstream to straighten the swirling flow. The configuration was designed within the EU Clean Sky 2 research project ASPIRE as a generic engine for numerical studies, representative of future UHBR turbofan. The nacelle, air-intake and nozzle shapes were delivered by Airbus, while the fan/OGV blades were designed by DLR based on specifications provided by Airbus (including specifications for the core flow). The nacelle features an air-inlet with a droop angle and a very small length-to-diameter ratio.

The aerodynamic conditions are the following: Mach number of 0.30, total pressure and temperature at zero altitude, which leads to a Reynolds number based on the nacelle diameter of around 6 million. The considered angles of attack vary between 15° and 40°, matching take-off conditions and enhance separation. The fan rotation is imposed at a rotation speed typical of take-off conditions. The mass-flow rate in the primary stream is the same for all angles of attack, as well as core pressure and temperature ratio.

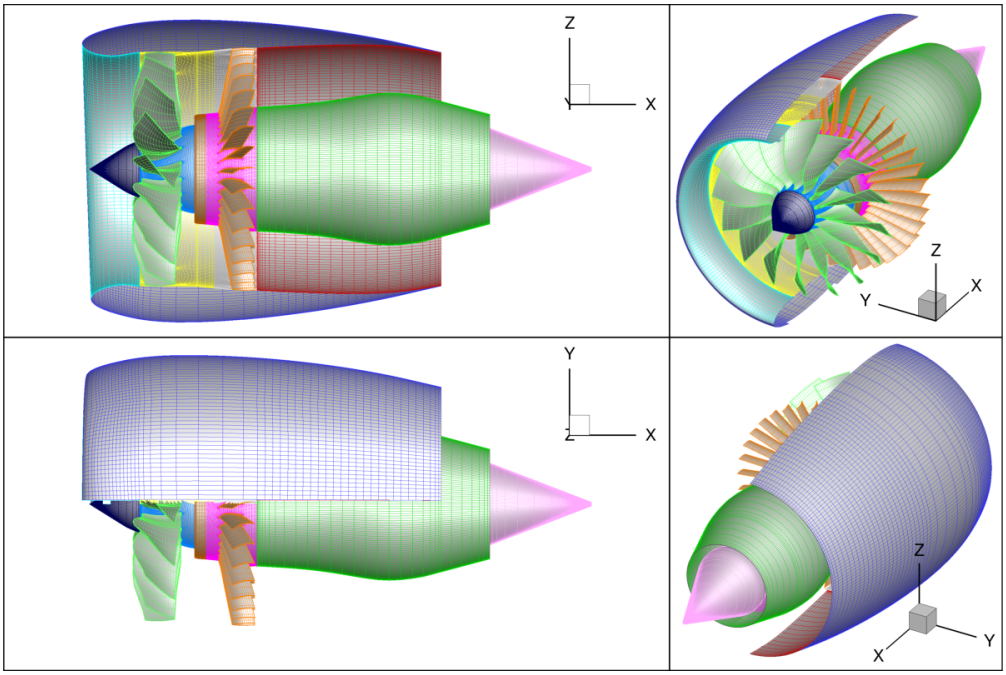

Figure 1. Numerical grid of the considered test case.

II.A. CFD simulation with *elsA*

The simulations were performed with the ONERA-Airbus-SAFRAN *elsA* software, whose developments are partially funded by Airbus, Safran, and ONERA which are co-owners of this software. It solves the compressible Navier-Stokes equations on structured, unstructured and hybrid multi-block grids using finite-volume formulation. For the simulations carried out in this study, the structured solver is used. Moving bodies are treated with mixing plane or sliding mesh condition, without Chimera. For the spatial integration, a second-order centred scheme is used for the diffusive fluxes, while the convective terms are treated with Roe scheme. The time integration is performed using an implicit backward Euler scheme, with second-order backward Gear scheme for the time-accurate simulations. The time step size allows to perform 16 iterations for each degree of fan rotation. This has been obtained imposing a number of time step per revolution equals to the number of fan blades, times the number of OGV blades times 10. For each time step, the number of sub-iterations is adjusted to reach a convergence of one order of magnitude of the inner iteration residuals. For the present simulations, this is usually the case after 5 to 10 Newton sub-iterations, depending on the grid refinement. A time-step convergence study is presented in section III to assess the possibility of using a coarser temporal definition.

The turbulence model used for all simulations is the k-ω Wilcox,[11] although other models like the k-ω with SST correction or the Spalart-Allmaras[12] with and without Quadratic Constitutive Relation (QCR) were considered for one specific angle of attack to check the impact of turbulence modelling on the solution.

Cassiopé(e) in-house software[13] is used for all pre- and post-processing operations. A coupling between *elsA* and Cassiopé(e) is used for on-the-fly post-processing during the time-accurate simulations. This allows the extraction of quantities like index of distortion, overall mass-flow rates at different locations, probes and wall-pressure distributions, essential for the evaluation of the engine performance during the simulations. All simulations were run in parallel on 112, 448 and 784 cores of the ONERA cluster for the coarse, medium and fine grids, respectively. The time needed to obtain each steady-state solution was around 3, 10 and 50 hours for the three levels of refinement, while in URANS the time needed to simulate a fan revolution was around 2, 6 and 28 hours. At least three fan revolutions are necessary to initialise the time-accurate solution, making the URANS simulation more than twice as expensive as the RANS. A typical simulation on the medium grid (steady-state computation and 8 fan revolutions for one angle of attack) takes roughly 25,000 CPU hours.

II.B. Meshing strategy

The nacelle is meshed alone with ANSYS ICEM/Hexa mesh generator, without the inner elements. The rest of the grid is obtained by rotating and duplicating each fan and OGV stage, meshed with Autogrid. The grid is refined at the walls consistently with the RANS modelling used for the attached boundary layers. Three grid levels (coarse, medium and fine) were tested in order to assess the mesh convergence of the different approaches. The sizes of the different grids are detailed in Table 1. The medium grid was defined by coarsening the fine grid by a factor 2 in each direction. The same approach was applied to build the coarse grid from the medium one. The y^+ value was set at 1 for the medium case. The choice was made to have 60 points in the boundary layer on the fine grid to have an accurate description of the boundary layers. The 36 OGV meshes lead to a number of azimuthal points close to 1,200 which ensures to correctly capture the interactions between fan and OGV blades. The decision was made to restrain to 800 points in the same direction for the nacelle mesh to limit the total size of the grid. Overall, the finest grid is composed of 250 millions nodes, and is shown in figure 1, where one over 8 points on the skin is represented. The medium and coarse grids are composed of 40 and 6 millions nodes, respectively. The domain size has 20 diameters upstream and downstream of the nacelle, 12.5 in the vertical direction.

	Coarse	**Medium**	**Fine**
Fan (rotating)	0.8 M	6.2 M	47.3 M
OGV (fixed)	0.6 M	4.1 M	31.5 M
Nacelle (fixed)	2.8 M	21.1 M	161.5 M
Total	4.2 M	31.4 M	240.2 M

Table 1. Number of million grid points for different levels of grid refinements.

II.C. Boundary conditions

The presence of the rotating fan implies that three interfaces between fixed and moving parts must be specified: the first between the nacelle intake and the fan face, the second between the end of the fan and the beginning of the OGV, and the last at the exit of the OGV, where the flow enters in the nozzle. In the case of steady-state computations, a mixing-plane boundary condition can be applied at these three interfaces: an azimuthal averaging is performed on the interface corresponding to the boundary and the averaged flow-field is transmitted from the upstream interface to the downstream one. For the URANS computations, an interpolation on the sliding mesh is performed in order to take into the account the unsteady effect. This sliding mesh method allows transporting the conservative and turbulent field of each grid point from one interface to the other one with great accuracy and is much cheaper than the overlapping blocks used when adopting the Chimera method. The main difference between the mixing plane and the sliding mesh condition is that the RANS approach can only be used with mixing plane. With this condition all the non symmetry in the flow filed are averaged in each of the three planes. This implies that the effect of the asymmetry of the nacelle, the incoming incidence of the flow, and the wakes of each blade are not transported between each interface. When performing a URANS simulation all informations are transferred from one interface to the other, allowing for a more accurate evaluation of the engine performance.

Since the combustion chamber is not present, primary flow inlet and outlet are modelled as boundary conditions. The total pressure and temperature are specified by the user. A coupling procedure is then adopted, allowing for an adjustment of the static pressure in order to achieve the desired mass-flow rate taking into the account the radial equilibrium due to the flow rotation.

II.D. Flow-control device

In the configuration with active control presented in section IV, boundary-layer suction through porous wall is proposed. First, based on the results of the clean case with the highest angle of attack, a zone in the intake is selected where the flow is the most separated. Then different sub-zones of the intake, with roughly the same size, are selected: these zones have two positions in the stream-wise direction (one down-stream close to the fan, the other upstream close to the nacelle lip), and four azimuthal extension. Figure 2 shows the summary of the selected cases. Each case is identified by two numbers: the first indicating the azimuthal

extent of the porous walls close to the fan and the second indicating those of the walls close to the nacelle lip. Shape of the porous walls is always symmetric with respect to the vertical symmetry plane of the nacelle.

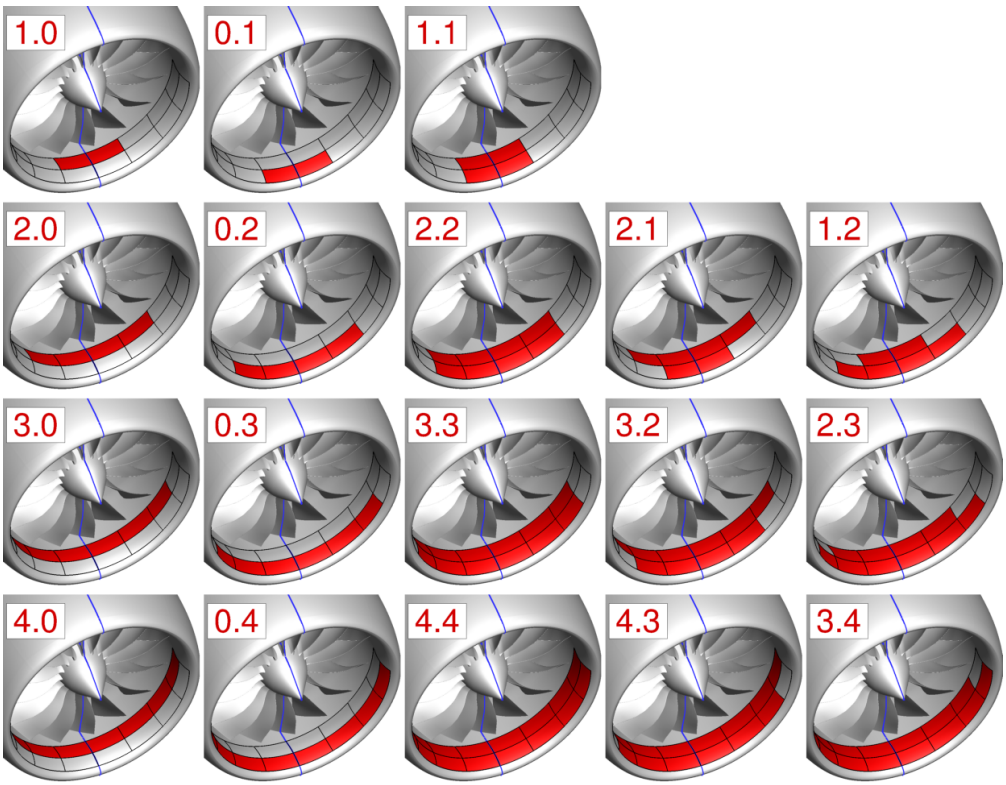

Figure 2. Location of the porous walls for active flow control and corresponding name of the configuration. The first number identifies the size of the porous wall in its most downstream position, the second the most upstream.

There are in total 18 configurations studied, all with the same suction velocity. In each configuration, the suction velocity is then increased, so that different mass-flow rates are obtained through the cavity.

III. Results without control

This section will present all the results for the configuration without flow control. Steady-state solutions are obtained with a mixing plane condition between the rotating fan and the fixed airframe. This approach allows to obtain a good estimation of the flow field taking into the account the rotating fan, without needing to actually perform any grid motion. The flow inside the nacelle will be axial-symmetric, and is used as starting point for the time-accurate simulations. Instantaneous and time-averaged unsteady solutions are then presented and the unsteady features of the flow are discussed. For both RANS and URANS simulations, the angle of attack is increased until massive separation is observed in the intake. Then, the case where the boundary layer is the most detached is selected for flow control and discussed in the next section. Grid refinement, turbulence model dependency and robustness of the results with respect to the time-step size are also investigated in this section.

Figure 3 presents the evolution of the Mach number on the $y = 0$ plane. The result is an instantaneous solution of time-accurate simulation on the medium grid for three angles of attack. Stream-traces are superposed to enhance the difference in the flow incidence and highlights the displacement of the stagnation point downstream while increasing the angle of attack.

Overall, the asymmetrical intake and the angle of attack of the incoming flow causes non-uniformity of the flow upstream of the fan. A supersonic region can be observed on the lower side of the nacelle, where a shock-induced separation appears at $\alpha = 40°$. The inlet flow accelerates around the inlet lip, resulting in a supersonic flow region followed by a shock. Previous studies have shown that a thinner leading edge shape is required in the short-inlet design to limit the external flow acceleration at cruise.[2] As a result, the over-speed along the inlet internal surface is increased at high-angles of attack. Local region of high Mach

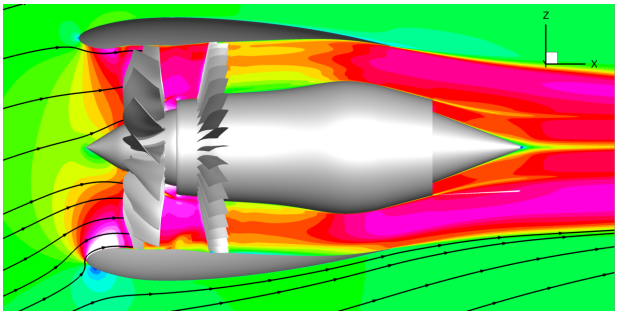

(a) $\alpha = 20°$.

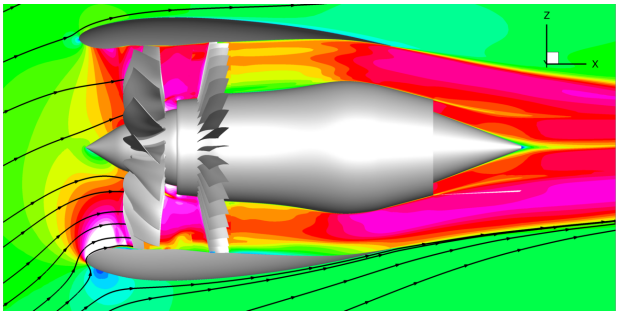

(b) $\alpha = 30°$.

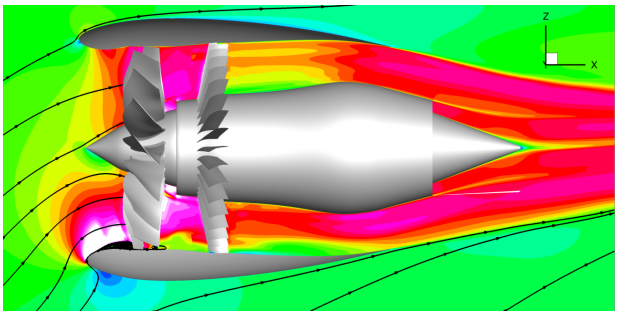

(c) $\alpha = 40°$.

Figure 3. Mach-number distribution on the symmetry plane of the engine for the medium grid.

number shifts toward the fan face, similarly to the cruise condition.

At low angles of attack, the flow can be considered fairly uniform inside the engine. Then, the separation is ingested by the fan and a deficit of velocity is transported through the OGV. Important differences can be seen for the most separated case between the upper and lower part of the secondary flow in the nozzle. The jet in the fan nozzle has also an influence on the primary stream, which however remains attached to the plug even for the highest angle of attack.

The main consequence of such a short intake is the proximity of the fan to the external flow. In nacelles with very short intakes, flow-through calculations indicate that the presence of the rotor increases the separation-free angle of attack, underlining the importance of capturing the influence of the rotor when studying fan-inlet coupling.[2] Furthermore, a comparison study between an isolated intake and a powered intake have shown that the fan stage has the beneficial effect of increasing tolerance to flow incidence and decreasing distortion.[14]

In figure 3(c) the jet-stream downstream of the nozzle bends upward because of the elevated angle of attack of this configuration. Separation is not observed on the external part of the nacelle.

Mass flow [kg/s]	**Coarse** Mix. Plane	**Coarse** Slid. mesh	**Medium** Mix. Plane	**Medium** Slid. mesh	**Fine** Mix. Plane	**Fine** Slid. mesh
$\alpha = 15°$	-1.05%	-0.92%	-0.02%	-0.14%	+0.19%	0.00%
$\alpha = 20°$	-1.31%	-1.23%	-0.20%	-0.39%	+0.02%	-
$\alpha = 25°$	-1.68%	-1.67%	-0.51%	-0.80%	-0.27%	-
$\alpha = 30°$	-2.41%	-2.45%	-1.14%	-1.64%	-	-
$\alpha = 35°$	-10.00%	-4.42%	-1.90%	-2.69%	-	-
$\alpha = 40°$	-13.43%	-8.70%	-3.59%	-5.57%	-	-

Table 2. Normalised mass-flow rate through the engine, effect of grid refinement for different angles of attack.

In order to compare global values obtained using the available grids at different angles of attack, Table 2 summarizes the results obtained using both steady-state simulations (thus with mixing-plane condition between fixed and rotating parts) and time-accurate simulations (thus with sliding-mesh approach). All

mass-flow rates have been divided by a reference value, that is the mass-flow rate obtained with the URANS simulation on the fine grid for $\alpha = 15°$.

Focussing on the first line of Table 2, it can be seen that the coarsest grid underestimates the mass-flow rate by 1%. On the contrary, the medium grid presents an excellent agreement with the results on the finest mesh. For this particular case at low angle of attack, the RANS solution yield values of mass-flow rates through the fan very similar to those predicted by the URANS simulation. The agreement deteriorates while increasing the angle of attack (first column of the table), which introduces asymmetries in the flow field that are not correctly transported using the mixing-plane approach.

Focussing on the last lines of Table 2, it can be seen that at high angle of attack the mass-flow rates are significantly lower than the reference value, obtained on the fine grid for $\alpha = 15°$. This behaviour is due to the flow separation on the lower part of the intake, which deteriorates the performance of the engine. Due to the unsteady effects, non captured by the RANS simulation, the solution obtained with mixing-plane condition predicts a sensitively different mass-flow rate with respect of the solution obtained with a URANS approach.

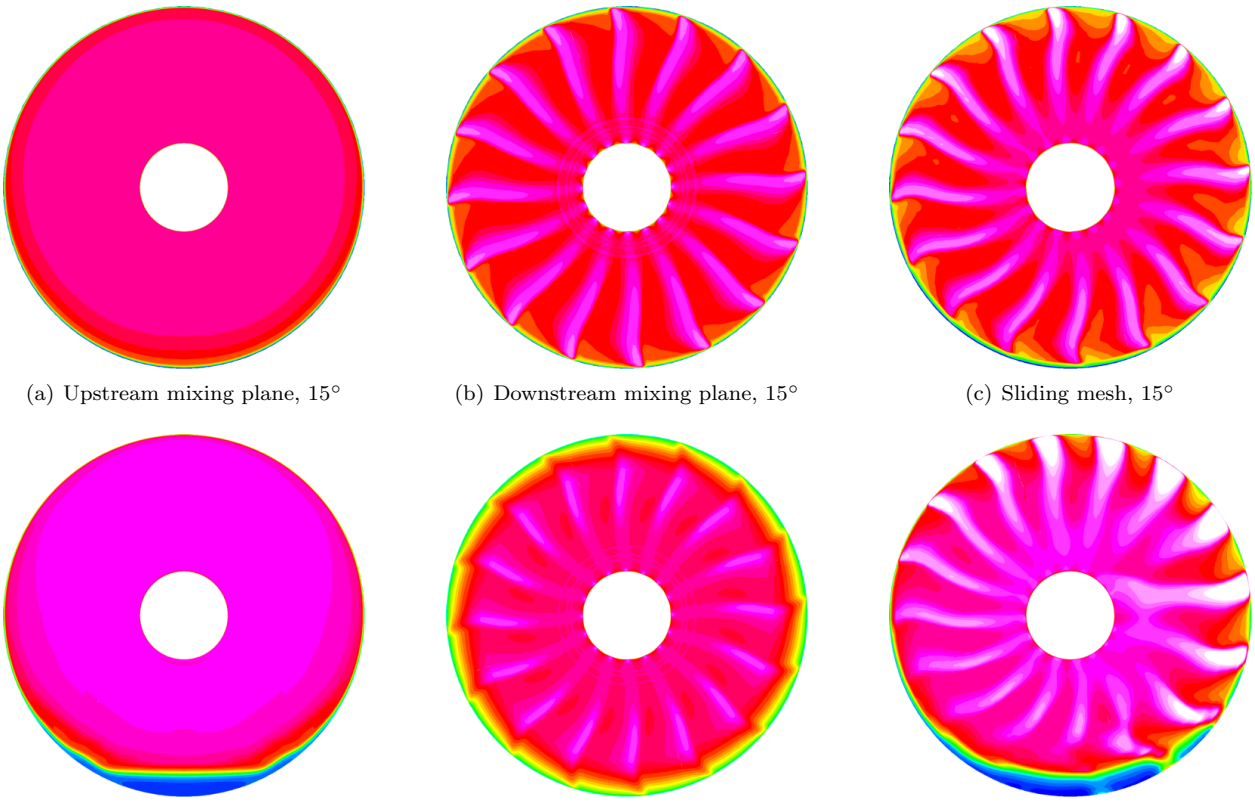

(a) Upstream mixing plane, 15° (b) Downstream mixing plane, 15° (c) Sliding mesh, 15°

(d) Upstream mixing plane, 40° (e) Downstream mixing plane, 40° (f) Sliding mesh, 40°

Figure 4. Total pressure distribution on the intake/fan interface: upstream the mixing plane (left), downstream (center) and on the sliding mesh window (right). Angle of attack $\alpha = 15°$ (top) and $\alpha = 40°$ (bottom), medium grid.

Figure 4 shows the evolutions of the total pressure in correspondence of the interface between the intake and the fan, obtained using different approaches. The figure presents on the top the configuration with the lowest angle of attack and on the bottom the configuration with $\alpha = 40°$. Figure 4(a), figure 4(b), figure 4(d) and figure 4(e) have been obtained with a RANS simulation, and show the distribution upstream and downstream the mixing plane. Figure 4(c) and 4(f) are an instantaneous result of the URANS simulation, obtained with the sliding mesh approach (the upstream and downstream planes are the same). On the top figures, when the angle of attack is small, no separation is present at the end of the intake. The flow is fairly symmetrical and RANS and URANS results (figure 4(b) and 4(c)) are similar. Obviously the trace of each fan blade is not visible upstream of the interface because their effect has been averaged by the mixing plane.

Figure 4(d), 4(e) and 4(f) present similar plots, obtained when $\alpha = 40°$. A separation on the lower part of the nacelle is visible figure 4(d), but the total-pressure loss are averaged by the mixing plane immediately downstream of the interface (figure 4(e)). The unsteady simulation with sliding mesh is necessary to simulate

the interaction between the separated zone upstream the interface and the rotating parts downstream of it. The RANS simulation in the rotating frame presented in figure 4(e) can capture the trace of each fan blade, but does not reproduce the separated flow in the intake. This artificial flow reattachment induced by the mixing plane is the reason why at high angle of attack the URANS simulation with sliding mesh is needed. Figure 4(f) presents an instantaneous result of the time-accurate simulation, where we can observe the interaction between the fan blade and the separated zone. In addition, the sliding-mesh approach allows to simulate the asymmetry of the flow, which is visible in the pressure distribution of the blades, which has higher peaks on the right side because of the rotating fan.

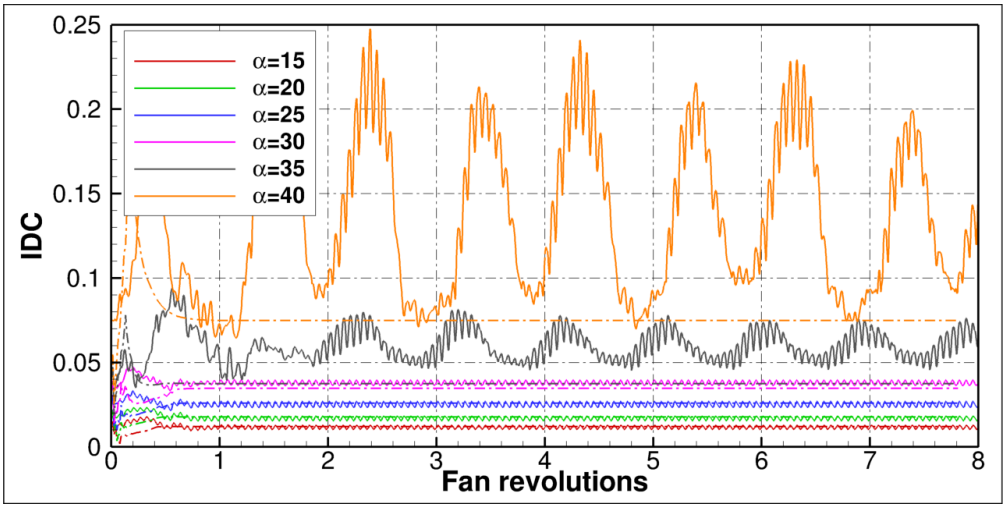

Figure 5. Evolution of the distortion coefficient upstream of the fan for different angles of attack.

The spatial evolution of the total pressure can be used to compute the distortion coefficient upstream of the fan. URANS simulations not only allow the use of the sliding mesh to accurately reproduce the interaction between the rotating and the fixing components, but give access also to a time-accurate solution. In those cases the distortion coefficient is a function of time and oscillates due to the rotation of the fan blades and due to the unsteady motions of the separated zones, if present. Figure 5 presents the circumferential distortion index (IDC) for various angles of attack, on a vertical plane at $y = -0.3m$, upstream of the fan. The figure presents the steady results obtained with RANS approach (dash-dotted line) as well as the time-accurate results obtained with URANS simulation (solid lines).

Figure 5 shows that, as previously mentioned, RANS and URANS results are in good agreement for low angles of attack. In the time-accurate solution, 16 peaks can be seen for each fan revolution period, indicating effect of the 16 fan blades. As the incidence is increased, the steady-state solution underestimates the distortion because of the failure to transport the separated zone from the intake to the the fan: this creates an artificial flow reattachment as consequence of the spatial averaging caused by the mixing plane. For the highest angles of attack ($\alpha = 35°$ and $\alpha = 40°$ of figure 5), the evolution of the IDC indicates also the presence of unsteady loads and flow non-uniformity that can cause periodic forcing on the fan blades, which can provoke fatigue failure. In the next session flow control will aim at reducing separation in order to increase the propulsion efficiency and also attenuate the unsteady loads.

Figure 6 presents the pressure coefficient (Cp) distribution on two blades for the case at $\alpha = 25°$. On the top, figure 6(a) and figure 6(b) have been obtained with a RANS simulation: the mixing plane approach yield a symmetric flow, so the same pressure coefficient is observed on all blades. Each line of the figure presents the pressure evolution obtained with a different turbulence model. It can be seen that the k-ω of Wilcox yields a result which is very similar to the one obtained using k-ω with SST correction. Similarly, the Spalart-Allmaras with and without QCR correction predict very close distribution. The results obtained with the k-ω models predicts a more downstream shock than the results obtained with the SA models. However, similar variations are observed for the pressure side of the profiles, so the estimation of the total lift produced by the blades is very close.

Figure 6(b) presents a similar plot, with Cp values closer to the fan shroud (90% of the radius). A similar behaviour is observed, with the k-ω models predicting a more downstream shock (close to the fan tip, a second shock is present also on the pressure side of the profile.

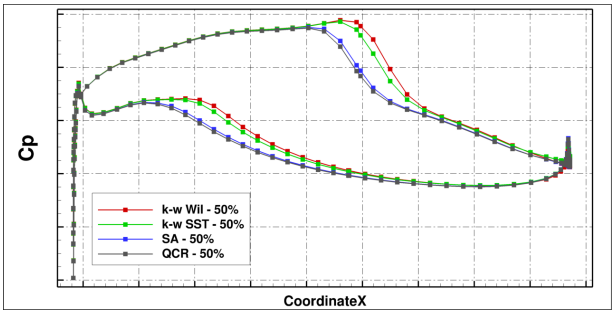

(a) Fan blade pressures with RANS simulation at 50% height.

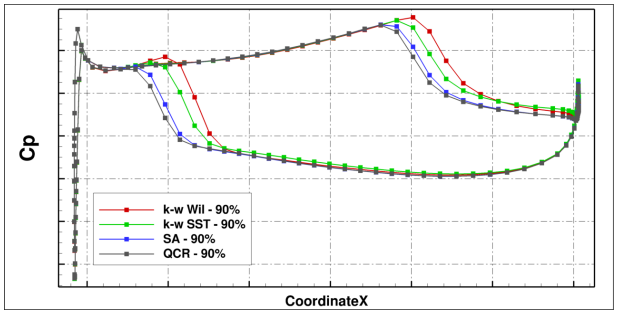

(b) Fan blade pressures with URANS simulation, 90% height.

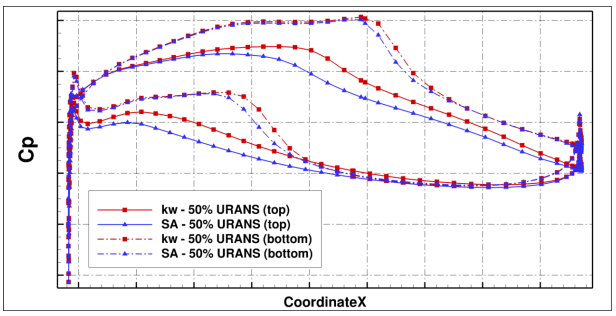

(c) Fan blade pressures with RANS simulation at 50% height.

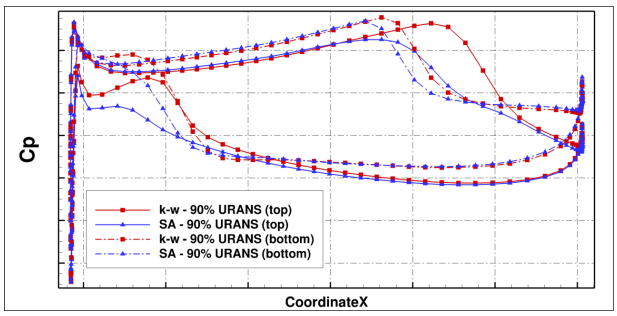

(d) Fan blade pressures with URANS simulation, 90% height.

Figure 6. Pressure coefficient on two different location on the fan blades in the highest and lowest position. Effect of the turbulence model for the case at $\alpha = 25°$, mixing plane (RANS) and sliding mesh (URANS) approach.

Two turbulence models have also been considered in URANS simulation, where the sliding mesh interface allows to represent the differences that can arise between a blade on the lower and upper part of the nacelle. Figure 6(c) presents a comparison of the pressure distribution at 50% of the radius: the effect of the turbulence model is small, while more differences can be seen when comparing a blade on the upper part of the nacelle with one on the lower part. A similar conclusion can be drawn for figure 6(d), presenting the pressure distribution closer to the fan tip.

Overall, despite some differences in the location of the shock wave, it is believed that the considered turbulence model give similar results, with the differences between the model less important than the differences due to the available approaches for modelling the interface between fixed and rotating parts of the engine.

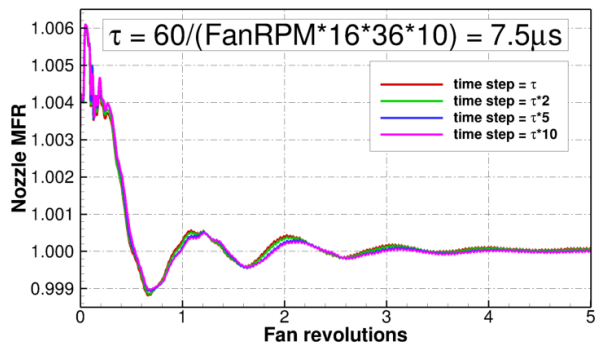

(a) Mass-flow rate through the fan for different time-step sizes.

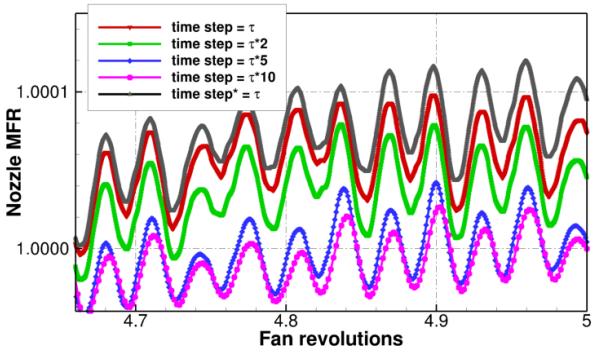

(b) Mass-flow rate through the fan, zoom.

Figure 7. Effect of the time-step size and convergence level of the inner-iteration in the time-resolved simulation.

Robustness of the results with respect to the time-step size are now investigated for the medium grid at $\alpha = 15°$. Figure 7 shows the evolution of the normalised mass-flow rate obtained when increasing the time-step size, measured downstream of the OGV. The reference time step is $\tau = 7.5\mu$s, which corresponds to 5760 steps per fan period. Figure 7 (a) indicates that a large time-step could have been used, allowing for

a cheaper simulation. However, Figure 7 (b) indicates that a slightly different behaviour is observed when focussing on the mass-flow rate oscillations in the wake of the OGV. The figure also presents the case where the time step has been kept the same as the reference, but more inner iterations have been performed to allow a further convergence between time steps: the difference in the evolution of the mass-flow rate is barely visible, so the chosen level of convergence is deemed correct.

IV. Results with active flow control

The results of the previous section have shown that despite some differences in the mass-flow rate and total-pressure distortion, the mixing plane condition can give a good appraisal of the flow field for all angles of attack in the complete configuration and particularly in the intake region where separation may occur. As mentioned before, this condition allows the use of RANS simulations to obtain a steady-state solution with limited costs. In this section the most separated case, corresponding to $\alpha = 40°$, is selected for flow control. RANS simulation is therefore used to define the most efficient configuration, which is then simulated in URANS to verify the effect of flow control using sliding-mesh approach on the interfaces between fixed and rotating elements.

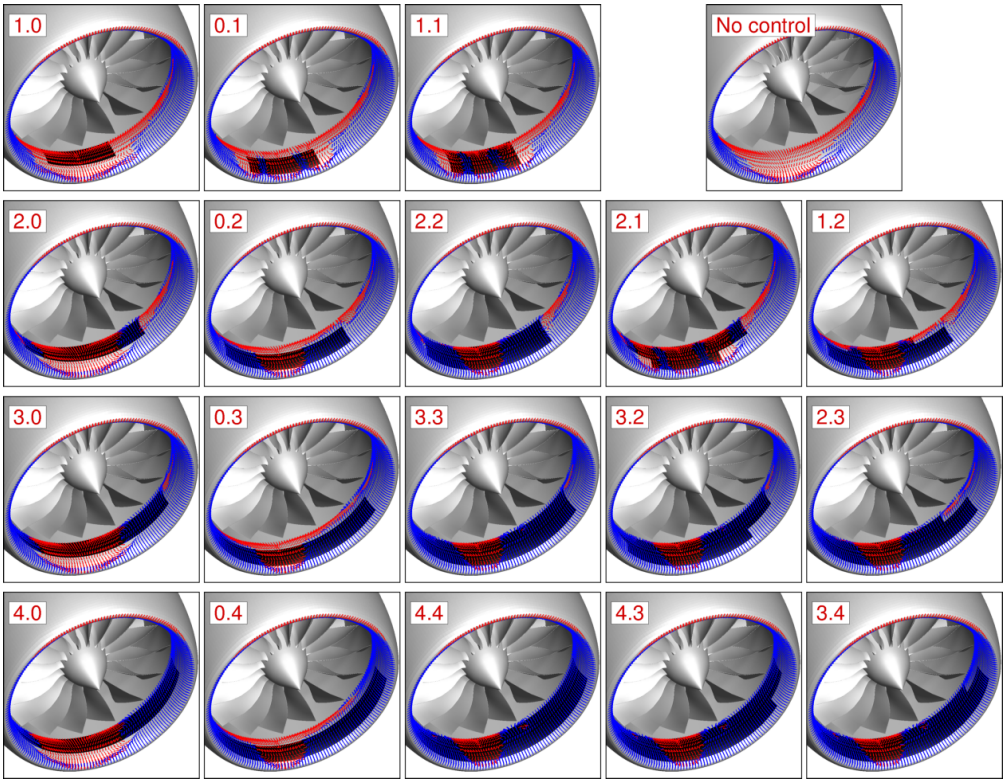

Figure 8. Skin-friction in the intake with control for different configurations, minimal suction velocity. The black region indicates the location of the porous wall. Vectors coloured by the stream-wise skin friction, separation in red.

The configuration considered in this study is an UHBR turbofan with a very short intake, designed for cruise conditions. Focussing on figure 3 (c), two main features can be observed on this particular configuration: the first one is that at high angle of attack, the separation of the boundary layer is induced by a shock wave that appears inside the nacelle. The second one is that the separation is interacting with the fan, which ingests the recirculation zone. Two conclusion can consequently be drawn: first, aspiration of the separated zone downstream of the shock can be a more efficient way of applying flow-control,[15] rather than upstream vortex generators or micro-jets, which are more adapted to leading-edge separations.[16] Second, the fan must be taken into the account for the evaluation of the flow-control effectiveness, since the reattachment points is determined by the interaction between the separation bubble and the fan blades in the lowest position.

A parametric study is here proposed on the complete configuration using the coarse grid, with mixing-

plane conditions. First, all cases presented in figure 2 are considered imposing the same uniform velocity magnitude through the porous wall. Most of the porosity parameters are taken from the characteristics of a typical control device, for example those used for hybrid laminar flow control: porosity coefficient of 8%, size of the holes of 1 mm with no inclination with respect to the wall normal and a wall thickness of 1 mm. Then, the velocity magnitude through the porous wall is increased and all results are compared between each other. For numerical reason, some of the cases with high suction velocity could not converge: those cases are not considered while looking for the optimal flow-control configuration.

Figure 8 shows the skin-friction inside the intake with control obtained for all considered configurations, with constant suction velocity equals to 8 m/s. The black region on the lower side of the nacelle indicates the location of the porosity (i.e. where the velocity through the wall is not equal to zero), as in figure 2. Vectors are coloured by the stream-wise skin-friction coefficient, and indicate where separation occurs. Whilst none of the selected case can completely suppress the separation, great reduction of the flow detachment with respect to the uncontrolled case (top right corner of figure 8) can be achieved by some configurations.

The most effective configurations seem to be those where the porous wall has a great extent, such for example those on the bottom right corner of figure 8. On the contrary, when the suction is in a zone with limited azimuthal extent (as for example in the first row of figure 8) or far from the nacelle lip (first column of figure 8), the separation is barely reduced from the case without control. Some interesting flow patterns arise when considering configurations with non-rectangular shapes, as for example in the last two columns of figure 8.

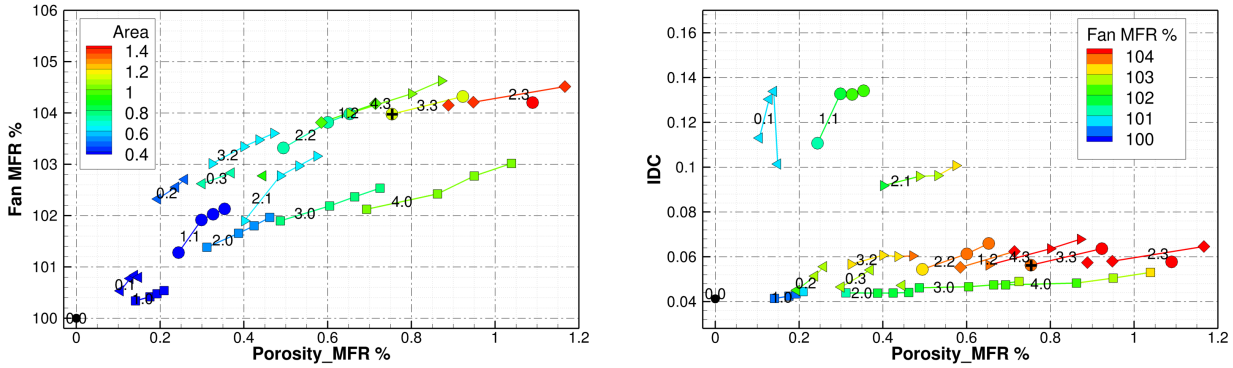

(a) Mass-flow through the fan vs. suction intensity.

(b) Distortion upstream the fan vs. suction intensity.

Figure 9. Result of the parametric study on the control device location, size and suction velocity.

When increasing the suction velocity the beneficial effect on the separation is also increased. Similar separation patterns remain for each configuration, but with a reduced size of the separated zone. In terms of performances of the engine, a smaller separation translates into a higher mass-flow rate through the fan, which is here considered as one of the key parameters to evaluate the effectiveness of the control device. However, when evaluating the global performance of the engine, one should take into the account also the fact that the suction velocity is directly linked to the mass-flow rate thorough the control device, which is not unlimited and free of costs. Since the different configurations considered have different extent of the porous zone, it is useful to compare the gain in mass-flow rate trough the fan to the mass-flow rate needed by the control device. This quantity is obviously linked to the suction velocity and the extent of the porous zone, but also depends on the location of the control device: strong density gradients are present in the shock-induced separation, so that a control device upstream of the shock will have, for a given suction velocity, less mass-flow rate than a control device placed on the supersonic region, because of the difference in density of the flow before and after the shock wave.

Figure 9 (a) shows a plot with the gain of mass-flow rate through the fan with respect to the uncontrolled region versus the mass-flow rate through the porous wall (normalised by the fan mass-flow rate). The configuration without control is represented by a black circle, with obviously no mass flow through the walls, and mass-flow rate of the fan equals to 100%. The figure indicates that an increase of the mass-flow rate through the control device has a positive effect on the engine performance. As indicated by the labels, each line of figure 9 (a) corresponds to a configuration of figure 2 or figure 8 , coloured by the surface of the porous wall (same symbols indicate same arrangement of the porous zone, as each column of figure 2). Some

interesting cases exist when the mass-flow of the control device is between 0.7% and 0.9%, where it can be more convenient to use higher suction velocity through a smaller surface rather than a larger surface with lower suction velocity. For reasons linked to the power available for the control device, the cases where the mass-flow rate is greater than 1% of the fan mass-flow rate are discarded.

Another important factor for the choice of the optimal control device is the total-pressure distortion of the flow upstream of the fan. Figure 9 (b) presents a comparison of the distortion index of all cases versus the mass-flow rate through the porous wall. The uncontrolled case is represented again by a black circle. The lines and dots, corresponding to the configurations as in figure 2, are coloured by the fan mass-flow rate, normalised by the mass-flow rates without control. It can be seen that the control device has a tendency to increase the distortion, especially when the fan mass flow is above 104%. However it should be kept in mind that the parametric study discussed in this section is based on RANS simulations with mixing plane conditions; as shown in figure 5, when massive separation is present the flow field is highly unsteady and the steady-state simulation underestimates the distortion.

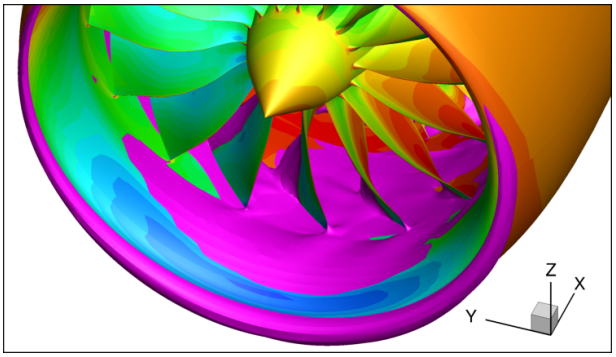

(a) Wall-pressure distribution with iso-surface of zero stream-wise velocity, without control.

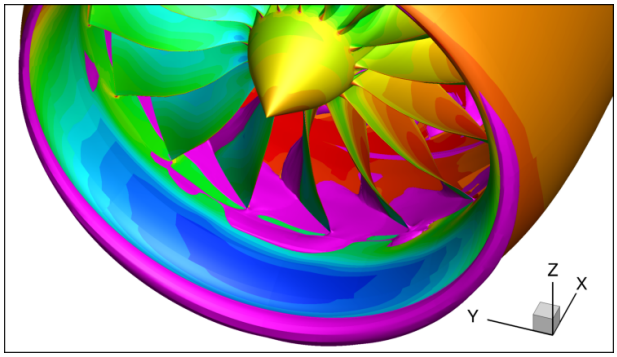

(b) Wall-pressure distribution with iso-surface of zero stream-wise velocity, with control.

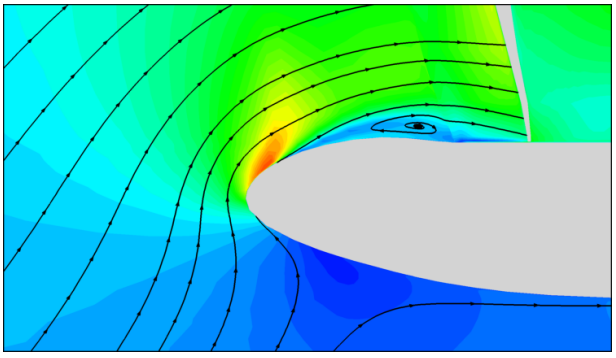

(c) Mach number on the plane $y = 0$, without control.

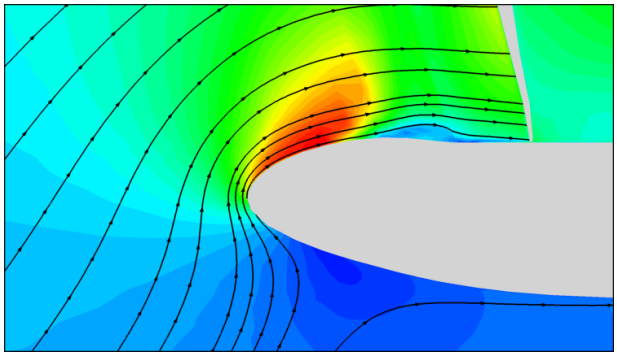

(d) Mach number on the plane $y = 0$, with control.

Figure 10. Time-accurate simulation, comparison at $\alpha = 40^\circ$ without (left) and with (right) control.

The selection of the best candidate for the flow control is made using the information on the two plots of figure 9. The case corresponding to *3.3* in figure 2 is considered the best compromise between cost, increase of performance and distortion. This particular case needs a flow rate thorough the porous wall corresponding to 0.75% of the fan mass flow and allows for an increase of 4% in the fan mass-flow, while keeping the distortion upstream of the fan lower than all other cases that deliver a greater increase in performance. This optimal point is highlighted in figure 9 by a black cross.

The optimal control location and suction velocity is then simulated in URANS with the sliding mesh approach. The result of the time-accurate simulation is presented in figure 10 and figure 11. Figure 10 (a) and 10 (b) present the wall-pressure distribution on the intake and fan for the case without and with control. An iso-surface of stream-wise velocity equals to zero indicates the flow separation, which is sensitively reduced in the case with flow control. The suction through the porous wall is not able to completely reduce the separation, especially close to the fan face, where the suction is not active. Small separations are also present in the most external part of the blades, especially those in the lowest azimuthal position. Another zone where separation persists is on the suction side of the fan blade in the lowest position. Figure 10 (c)

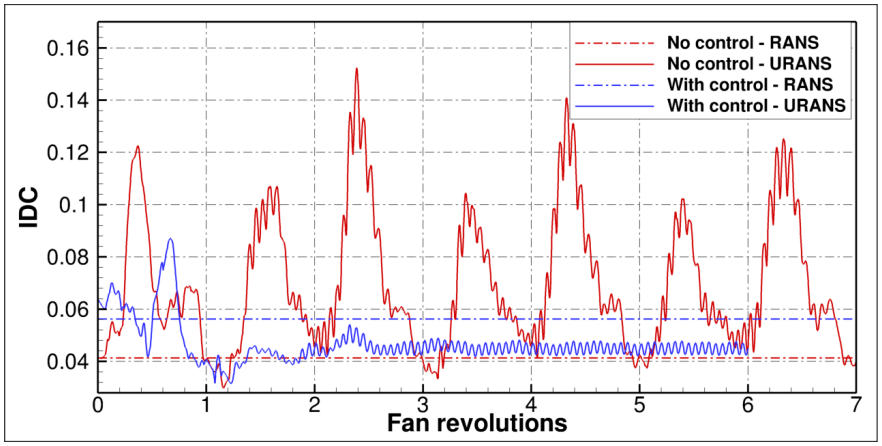

Figure 11. Evolution of distortion coefficient at $\alpha = 40°$ with and without flow control.

and figure 10 (d) presents the Mach-number distribution on the symmetry plane located in $y = 0$. Similar flow fields have been observed in a previous study when investigating the behaviour of ultrashort nacelles for low fan-pressure-ratio propulsors.[2] The separation in the controlled case has a reduced size, allowing for a greater supersonic region inside the nacelle. In the case with suction through the porous wall, more horizontal stream-traces indicate that the intake is more effective in straightening the flow before the fan.

Figure 11 presents the distortion coefficient upstream of the fan for the case with and without control. As indicated in figure 9 (b), the RANS solution indicates that the control device increases the distortion. However, the more accurate URANS simulation indicates the opposite, proving the effectiveness of the proposed flow-control technique. Moreover, the time-accurate simulation not only indicates that the controlled case has a lower averaged distortion, but the peaks corresponding to the unsteady motions of the separated zone are no longer present. A comparison with figure 5 shows that the level of distortion is comparable to the case at $\alpha = 30°$, where figure 3 (b) indicated similar separation sizes.

V. Conclusion and Outlook

Requirements of fuel efficiency and environmental impact have rose the interest towards the UHBR engines. Increasing the values of bypass ratio leads to major modifications of the fan and the nacelle, which will have intakes with large diameters and reduced lengths. In order to allow the design of engines with great performances, CFD codes must provide reliable tools able to accurately predict the flow field and the strong interactions between the elements composing the engine. In off-design conditions, this new type of engine could be subject to undesirable separation, and active flow control could be used to assure the operability of the intake even in presence of massively separated flow.

In this paper an isolated engine representative of a UHBR turbofan is numerically investigated. Intake, fan, OGV and nozzle were present in the numerical grid, with rotating bodies fully modelled. Three levels of grid refinement and various turbulence models were considered to assess convergence and robustness of the results. The configuration has been considered in RANS simulation, with steady-state solutions obtained using mixing plane between fixed and rotating parts providing a quick estimation of the flow-field. Unsteady simulations have then been completed, using sliding-mesh approach to accurately predict the time-resolved behaviour of the engine. Overall, mixing-plane plane simulations can be considered relatively quick and cheap, but not adapted to cases with separation, since they do not allow to capture non-symmetric features of flow. However, despite some differences in the mass-flow rate and total-pressure distortion, the mixing plane condition can give a good appraisal of the flow-field for all angles of attack in the complete configuration and particularly in the intake region where separation may occur. For a more accurate prediction of the flow, URANS simulations with sliding-mesh between fixed and rotating parts must be used. Parallel computations have shown the ability of modern codes to handle complex simulations and estimate the performance of those engine where the interaction between all elements composing the turbofan play a central role.

The UHBR turbofan has been simulated in take-off conditions at increasing angles of attack. Separation-free flow is observed at low incidence, while at high incidence the intake, optimised for cruise conditions, does

not present a typical leading-edge separation but more a shock-induced separation inside the nacelle. Due to the limited length of the intake, the proximity of the rotating fan to the nacelle lip, typical in this particular UHBR configuration, has a beneficial effect on the separated zone, allowing the flow to re-attach even at high angles of attack. A further increase in the incidence causes massive separation to appear, with dramatic unsteady effects on the flow distortion. In this case, flow control can be applied to limit the undesirable effects, with aspiration of the separated zone downstream of the shock, using a porous wall that could be fitted in the intake. This technique can be more efficient than control by upstream vortex generators or micro-jest, which is more adapted to leading-edge separation. A parametric study has thus been proposed in order to find the optimal location of the control device using steady-state simulation, and a time-accurate result has been compared with the case without control in order to evaluate the performance of the proposed device.

It has been shown that the control device has a positive effect on the total mass-flow rate of the engine thanks to a reduction of the separated zone, which is proportional to the suction velocity. However, the distortion upstream of the fan can be increased by too powerful control devices. Overall, it has been shown that suction from a porous wall can provide a beneficial effect on the intake at very high angle of attack where massive separation occurs. The next steps will be a comparison with experimental data in order to validate the numerical results and a study on the implementation and integration concept in order to provide an evaluation at aircraft level.

Acknowledgements

The studies presented in this article have used the ONERA-Airbus-SAFRAN elsA software whose development is partially funded by Airbus, Safran and ONERA, which are co-owners of this software. This project has received funding from the Clean Sky 2 Joint Undertaking under the European Union's Horizon 2020 research and innovation program under grant agreement No 681856-2 - ASPIRE.

References

[1]Burlot, A., Sartor, F., Vergez, M., Méheut, M., and Barrier, R., "Method comparison for fan performance in short intake nacelle," *2018 AIAA AVIATION Forum. 25–29 June 2018 Atlanta, Georgia*, 2018.

[2]Peters, A., Spakovszky, Z., Lord, W., and Rose, B., "Ultrashort Nacelles for Low Fan Pressure Ratio Propulsors," *Journal of Turbomachinery*, Vol. 137, 2015, pp. 1–14.

[3]Gad-el Hak, M., *Flow Control: Passive, Active, Reactive Flow Management*, Cambridge Univ Press, 2000.

[4]McLean, J., Crouch, J., Stoner, R., Sakurai, S., and Seidel, G., "Study of the application of separation control by unsteady excitation to civil transport aircraft," *NASA CR-1999-209338*, 1999.

[5]Callender, B., Gutmark, E. J., and Martens, S., "Far-field acoustic investigation into chevron nozzle mechanisms and trends," *AIAA journal*, Vol. 43, No. 1, 2005, pp. 87–95.

[6]Henderson, B., "Fifty years of fluidic injection for jet noise reduction," *International Journal of Aeroacoustics*, Vol. 9, No. 1-2, 2010, pp. 91–122.

[7]Krishnan, K., Bertram, O., and Seibel, O., "Review of hybrid laminar flow control systems," *Progress in Aerospace Sciences*, Vol. 93, 2017, pp. 24 – 52.

[8]Yousefi, K. and Saleh, R., "Three-dimensional suction flow control and suction jet length optimization of NACA 0012 wing," *Meccanica*, Vol. 50, No. 6, Jun 2015, pp. 1481–1494.

[9]Bur, R., Corbel, B., and Délery, J., "Study of passive control in a transonic shock wave/boundary-layer interaction," *AIAA journal*, Vol. 36, No. 3, 1998, pp. 394–400.

[10]Cambier, L., Heib, S., and Plot, S., "The ONERA elsA CFD software: input from research and feedback from industry," *Mechanics and Industry*, Vol. 14, 1 2013, pp. 159–174.

[11]Wilcox, D., "Reassessment of the scale-determining equation for advanced turbulence models," *AIAA journal*, Vol. 26, No. 11, 1988, pp. 1299–1310.

[12]Spalart, P. R. and Allmaras, S. R., "A one equation turbulence model for aerodinamic flows," *AIAA journal*, Vol. 94, 1992.

[13]Benoit, B., Péron, S., and Landier, S., "Cassiopee: A CFD pre- and post-processing tool," *Aerospace Science and Technology*, Vol. 45, 2015, pp. 272–283.

[14]Carnevale, M., Wang, F., S. Green, J., and Di Mare, L., "Lip Stall Suppression in Powered Intakes," *Journal of Propulsion and Power*, Vol. 32, 2016, pp. 161–170.

[15]Keerthi, M. and Kushari, A., "Effectiveness of vortex generator jets and wall suction on separated flows in serpentine-duct diffuser," *Aerospace Science and Technology*, Vol. 34, 2014, pp. 12 – 19.

[16]Wakelam, C., T.P., H., Hodson, H., Evans, S., and Chanew, P., "Separation Control for Aeroengine Intakes, Part 1: Low-Speed Investigation of Control Strategies," *AIAA journal*, Vol. 28, No. 4, 2012.